

Autoionization of high- ℓ core-excited Rydberg states of alkaline-earth-metal atoms

E. Marin-Bujedo and M. Génévriez*

*Institute of Condensed Matter and Nanosciences,
Université catholique de Louvain, BE-1348 Louvain-la-Neuve, Belgium*

(Dated: July 7, 2023)

The autoionization of core-excited Rydberg states is theoretically studied for a broad range of principal and angular-momentum quantum numbers n and ℓ in alkaline-earth-metal atoms. We combined two theoretical methods to calculate accurate autoionization rates for $n = 10 - 65$ and $\ell = 0 - 45$ over the 100 orders of magnitude that they span. The strong interaction between the two valence electrons for low ℓ states is treated from first principles with configuration interaction with exterior complex scaling, while at large ℓ the weak correlation is described by a perturbative approach and arbitrary-precision floating-point arithmetics. The results, which we benchmark against available experimental data, provide autoionization rates for the $Np_{1/2,3/2}$ and, when applicable, $(N-1)d_{3/2,5/2}$ ion-core states of Mg, Ca and Sr ($N = 3 - 5$). Using the extensive set of calculated data, we analyze the dependence of the rates on ℓ and identify five general laws of the autoionization of high- ℓ states. An empirical formula describing the scaling of the rates with ℓ is suggested.

I. INTRODUCTION

When the ion core of a Rydberg atom or molecule is excited the system can decay via three different mechanisms: fluorescence of the ion core, fluorescence of the Rydberg electron, and, because the energy of the system is above the first ionization threshold, autoionization. Between these three mechanisms, autoionization is the fastest by up to several orders of magnitude for states in which the orbital angular momentum of the Rydberg electron is low [6]. The dynamics governing autoionization are a sensitive probe to electron correlations and, as such, have been extensively studied both in the time and frequency domain [1–3]. Experiments based on ion-core excitation [4] have unraveled some of the fascinating electron dynamics that take place in the dense manifolds of core-excited Rydberg states [5–9], and studies are ongoing to probe the complex correlations that occur for even higher degrees of core excitation [10, 11]. The development of multi-channel quantum defect theory has led to a clear and powerful way of understanding autoionization as the inelastic scattering of the Rydberg electron off the ion core. An alternative method, the configuration interaction with exterior complex scaling (CI-ECS), was recently used [11–13] to describe the dynamics of core-excited Rydberg states, in particular for higher-lying core excitation where it provided a spectacular visualization of electron dynamics [14].

The behavior of autoionization when the Rydberg electron has a low orbital-angular-momentum quantum number ℓ has been extensively studied (see, *e.g.*, Refs. [6, 15] for reviews). In the absence of series perturbations, the autoionization rates of a given series, converging to a given ion-core state, scale with the principal quantum number of the Rydberg electron as n^{-3} [15]. This scaling is no more than the probability to find the Rydberg elec-

tron near the nucleus, which is where the Rydberg electron inelastically scatters off the ion core and autoionizes. Autoionization for states with high ℓ values, on the other hand, is much less well characterized. The centrifugal barrier

$$\frac{\ell(\ell+1)}{2r^2} \quad (1)$$

prevents the penetration of the Rydberg-electron wavefunction into the ion core region, thereby suppressing autoionization. Pioneering experimental studies in Sr have shown that the rates indeed drop rapidly with ℓ [4], a result that was later verified for other series and species [16–19] and confirmed by theoretical predictions for $\ell \lesssim 10$ [19–21]. Fluorescence-decay mechanisms have been observed to dominate the decay of core-excited Rydberg states for sufficiently high ℓ values [3]. While values or upper limits of the autoionization rates have been measured for ℓ as high as 50 [18], theoretical values for $\ell \gtrsim 10$ are lacking, a fact that can be attributed to the difficulty of calculating the matrix elements involved in the rates.

The autoionization rates of high- ℓ core-excited Rydberg states play an important role in pulsed-field-ionization zero-kinetic-energy photoelectron spectroscopy [22, 23]. Their low values stabilize core-excited Rydberg states against autoionization [24], which permits the measurement of photoelectron spectra of atoms, molecules and ions at high resolution [22, 25, 26]. Autoionization also has significant interest in cold-atoms experiments where it has been used to image ultracold Rydberg gases [27], track the formation of ultracold neutral plasmas [28] or realize high-fidelity state detection of Rydberg atoms in an atomic array [29]. The possibility to suppress autoionization offers many interesting properties for quantum optics and quantum information experiments with Rydberg atoms [30]. Ion-core fluorescence, which can only be observed if it is faster than autoionization, has been used to image ultracold Rydberg gases [31], and optical control of the ion core is a

* matthieu.genevriez@uclouvain.be

promising route to manipulate Rydberg atoms without perturbing the Rydberg electron [32–34]. In these perspectives, it appears desirable to better understand the behavior of autoionization with ℓ , from regions where it predominates over other decay rates to regions where it is completely suppressed.

We present a theoretical study of the autoionization of alkaline-earth-metal atoms (Mg, Ca, Sr) in core-excited Rydberg states. These species were chosen for two reasons. First, they are widely used in the quantum optics and quantum information applications mentioned above. Second their electronic structure is both amenable to high accuracy calculations and simple enough so that the different dynamics governing autoionization can be identified and understood.

We developed and used two theoretical methods to calculate autoionization rates from $\ell = 0$ all the way to $\ell = 45$, for $n = 10 - 65$ and for ion-core states comprising the excited states $Np_{1/2}$, $Np_{3/2}$, and, when applicable, $(N - 1)d_{3/2}$ and $(N - 1)d_{5/2}$ ($N = 3, 4$ and 5 for Mg, Ca and Sr, respectively). The relevant energy-level structures and energy values of the three species are summarized in Fig. 1. To calculate the rates over such a broad range of states, we combined the capability of CI-ECS [12, 14, 35] to treat the complete two-electron dynamics from first principles with a perturbative treatment of electron correlations to calculate the extremely small autoionization rates of high- ℓ states with arbitrary numerical precision. The two methods are discussed in detail in Sec. II. The results, presented in Sec. III, provide a complete picture of the autoionization rates of the core-excited Rydberg states of Mg, Ca and Sr. They allow us to identify general trends and properties of the autoionization of high- ℓ states, which we rationalize by investigating the underlying electron dynamics. An empirical formula describing the scaling of the rates with ℓ is suggested.

II. THEORY

A. CI-ECS calculations

The description of core-excited Rydberg states is a challenging task for atomic-structure techniques because it requires to treat the electronic motion far from the nucleus ($r \sim 3000 a_0$ for $n = 45$), to calculate electronic correlations over large regions of configuration space, and to describe continuum processes and resonances. As in other studies (see Ref. 6 for a review), we reduce the complexity of the problem by treating alkaline-earth-metal atoms as quasi two-electron systems. The two valence electrons, subject to the effective field of the closed-shell doubly charged ion core, are considered explicitly. The effect of the remaining electrons, on the other hand, is accounted for with a fitted effective core model potential. The effective Hamiltonian describing the two va-

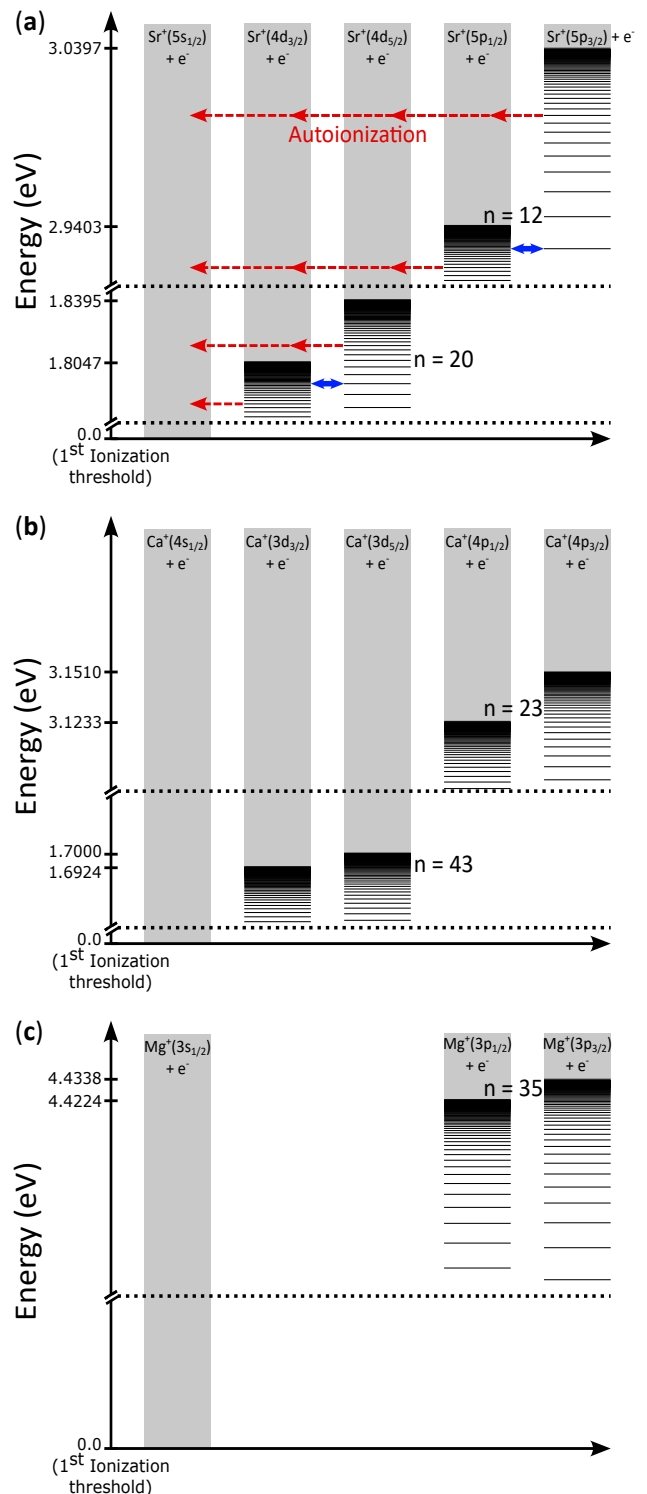


FIG. 1. (a) Energy-level scheme of the relevant Rydberg states of Sr. The vertical scale is discontinuous. The red arrows represent autoionization processes. The blue double arrows illustrate other possible channel interactions between adjacent Rydberg series, responsible for series perturbations. For each ion-core fine-structure multiplet, we indicate the principal quantum numbers below which spin-orbit autoionization into the continua above the lowest fine-structure component is no longer possible. Same energy-level scheme for Ca (b) and Mg (c).

lence electrons is given by

$$\hat{H}(\mathbf{r}_1, \mathbf{r}_2) = -\frac{1}{2}\nabla_1^2 - \frac{1}{2}\nabla_2^2 + V_{\ell_1}(r_1) + V_{\ell_2}(r_2) + \frac{1}{r_{12}} + V_{\ell_1 j_1}^{\text{SO}}(r_1) + V_{\ell_2 j_2}^{\text{SO}}(r_2) + V_{\text{pol}}^{(2)}(\mathbf{r}_1, \mathbf{r}_2), \quad (2)$$

where the vectors \mathbf{r}_1 and \mathbf{r}_2 represent the positions of the two electrons and r_{12} is the distance between them. The Hamiltonian includes ℓ -dependent model potentials $V_{\ell_i}(r_i)$ representing the effect of the doubly charged ion core on the valence electrons independently ($i = 1, 2$). It also includes the electron repulsion $1/r_{12}$ and the spin-orbit interaction $V_{\ell_i j_i}^{\text{SO}}(r_i)$, with j_i the total-angular-momentum quantum number of each electron. The two-electron term $V_{\text{pol}}^{(2)}(\mathbf{r}_1, \mathbf{r}_2)$ represents the polarization of the core upon the concerted motion of the two electrons [12, 36, 37].

The model potentials $V_{\ell}(r)$ are of the form proposed in Ref. 6,

$$V_{\ell}(r) = -\frac{1}{r} \left[2 + (Z-2)e^{-\alpha_1^{\ell} r} + \alpha_2^{\ell} e^{-\alpha_3^{\ell} r} \right] - \frac{\alpha_{\text{cp}}}{2r^4} W_6(r; r_c^{\ell}), \quad (3)$$

with the cutoff function W_6 defined as

$$W_6(r; r_c^{\ell}) = 1 - e^{-(r/r_c^{\ell})^6}. \quad (4)$$

The parameters α_1^{ℓ} , α_2^{ℓ} , α_3^{ℓ} and r_c^{ℓ} have been optimized on the experimental values of the energy levels of the singly-charged ion in Refs. [38], [6] and [37] for Mg^+ , Ca^+ and Sr^+ , respectively. Their values are listed in Table I.

The spin-orbit interaction is given by [6]

$$V_{\ell j}^{\text{SO}}(r) = \alpha_{\text{SO}}^{\ell} \frac{\alpha^2}{2} \boldsymbol{\ell} \cdot \mathbf{s} \frac{1}{r} \frac{dV_{\ell}}{dr} \left[1 - \frac{\alpha^2}{2} V_{\ell}(r) \right]^{-2}, \quad (5)$$

with α the fine-structure constant. The additional scaling factor $\alpha_{\text{SO}}^{\ell}$ was introduced and adjusted to reproduce the spin-orbit splittings of the low-lying excited states of the ion with an accuracy of better than 1 cm^{-1} , instead of the 10 cm^{-1} accuracy obtained without it. Its values are also given in Table I. The 1-cm^{-1} accuracy is required to predict perturbations of the energies and autoionization rates caused by Rydberg states of adjacent series with sufficient accuracy (see Ref. 35 for examples with Mg). Without it, the perturbations would occur at the wrong energies and therefore for the wrong Rydberg states.

The two-electron Schrödinger equation associated with the Hamiltonian (2) is solved using the CI-ECS method, which has been described in detail elsewhere [12, 14, 35]. Briefly, the two-electron wavefunction is written as a linear combination of anti-symmetrized products of one-electron spin-orbitals. Angular momenta are coupled in the jj coupling scheme, which is the most appropriate for core-excited Rydberg states [6]. Autoionization and

TABLE I. Model-potential parameters used in the calculations reported in this work.

	α_1^{ℓ}	α_2^{ℓ}	α_3^{ℓ}	r_c^{ℓ}	α_{cp}	$\alpha_{\text{SO}}^{\ell}$
	Mg					
$\ell = 0$	4.51367	11.81954	2.97141	1.44776	0.49	1
$\ell = 1$	4.71475	10.71581	2.59888	1.71333	0.49	0.7875
$\ell \geq 2$	2.99158	7.69976	4.38828	1.73093	0.49	1
	Ca					
$\ell = 0$	4.0616	13.4912	2.1539	1.5736	3.5	1
$\ell = 1$	5.3368	26.2477	2.8233	1.0290	3.5	0.984
$\ell = 2$	5.5262	29.2059	2.9216	1.1717	3.5	0.68
$\ell \geq 3$	5.0687	24.3421	6.2170	0.4072	3.5	1
	Sr					
$\ell = 0$	3.86849	7.89363	1.82951	1.11292	5.3	1
$\ell = 1$	3.43901	2.74445	1.48442	1.22661	5.3	0.982
$\ell = 2$	3.39035	4.32782	1.58635	1.55384	5.3	0.844
$\ell \geq 3$	4.81077	4.06763	1.75544	0.94593	5.3	1

other continuum processes are treated using the technique of exterior complex scaling (ECS) [39, 40]. Following ECS, the radial coordinates r_1 and r_2 of the electrons are rotated into the complex plane by an angle θ beyond a radius R_0 ,

$$r \rightarrow \begin{cases} r & \text{if } r < R_0 \\ R_0 + (r - R_0) e^{i\theta} & \text{if } r \geq R_0 \end{cases}. \quad (6)$$

The interest of ECS lies in the behavior of resonance wavefunctions. For real r values, the amplitudes of resonance wavefunctions are nonnegligible even as $r \rightarrow \infty$. Upon complex scaling, these become exponentially damped at large distances and can be represented by square-integrable functions. Calculations can thus be performed in a box of finite radius r_{max} even when continua are involved. The size of the box limits the spatial extent of the largest Rydberg wavefunction that can be represented, and therefore gives an upper bound to the maximal n value that can be reliably calculated. We typically choose $r_{\text{max}} > 10\,000 a_0$ (see Table II) such that $n_{\text{max}} \gtrsim 70$.

Complex scaling requires the use of complete square-integrable basis sets, which would make the size of the two-electron basis set very large and the calculations computationally demanding (see, *e.g.*, Ref. [41]). This issue is overcome by choosing the complex-rotation radius R_0 to be larger than the extension of the core-electron wavefunction. In that case the core electron does not reside in the complex-scaled region and is well described by a small number of radial functions. Only the outer electron must be described by a (quasi)complete basis set and the size of the two-electron basis set is dramatically reduced.

In practice, the one-electron spin-orbitals entering the two-electron wavefunction are constructed from radial functions, spherical harmonics and spinors (see [12]

TABLE II. FEM-DVR parameters used in the CI-ECS calculations reported in this work.

Element	$[r_i, r_{i+1}]$ (a_0)	N_i	θ_i ($^\circ$)
Mg			
$i = 1$	[0, 100]	100	0
$i = 2$	[100, 17600]	550	5
Ca			
$i = 1$	[0, 10]	70	0
$i = 2$	[10, 250]	70	0
$i = 3$	[250, 10250]	300	5
Sr			
$i = 1$	[0, 10]	80	0
$i = 2$	[10, 150]	80	0
$i = 3$	[150, 13150]	350	5

TABLE III. Core-electron orbitals included in the CI-ECS calculations reported in this work.

Atom	Core-electron orbitals
Mg	$3s_{1/2}, 3p_{1/2,3/2}, 3d_{3/2,5/2}, 4s_{1/2}, 4p_{1/2,3/2}$
Ca	$4s_{1/2}, 3d_{3/2,5/2}, 4p_{1/2,3/2}, 5s_{1/2}, 4d_{3/2,5/2}, 5p_{1/2,3/2}, 4f_{5/2,7/2}, 5d_{3/2,5/2}, 5f_{5/2,7/2}$
Sr	$5s_{1/2}, 4d_{3/2,5/2}, 5p_{1/2,3/2}, 6s_{1/2}, 5d_{3/2,5/2}, 6p_{1/2,3/2}, 4f_{5/2,7/2}, 7s_{1/2}, 6d_{3/2,5/2}, 7p_{1/2,3/2}$

for details). The complex-scaled radial functions describing each of the two electrons are numerical finite-element discrete-variable-representation (FEM-DVR) functions [35, 42]. They are obtained by solving the one-electron radial Schrödinger equation for the singly-charged ion along the complex ECS contour (6). In the FEM-DVR method, the radial space is split into several finite elements $[r_i, r_{i+1}]$ and, in each element i , the Schrödinger equation is solved on a grid of N_i points with a Legendre-Gauss-Lobatto DVR method [43]. We carefully chose the size of the finite elements and the number of grid points to minimize the basis-set size and make the calculations as fast as possible. The parameters of the FEM-DVR calculations are listed in Table II for each alkaline-earth-metal atom considered in this work.

In the CI expansion of the two-electron wavefunction, we use the quasi-complete set of $1 + \sum_i (N_i - 1)$ FEM-DVR radial functions to describe the Rydberg electron. The set of FEM-DVR functions representing the core electron is restricted to those describing the low-lying levels of the Mg^+ , Ca^+ and Sr^+ ions listed in Table III. Together, this means that the two-electron basis set comprises from 5 000 to 30 000 basis functions depending on the total angular momentum, the parity, and the atomic species.

The Hamiltonian matrix (2) is calculated along the ECS contour with the complex-scaled FEM-DVR basis and diagonalized. The eigenvalues and eigenstates of the

Hamiltonian are attributed, by inspecting the coefficients of the CI expansion, to a Rydberg series with given values of N , ℓ_1 , j_1 , ℓ , j and J . The quantum numbers N , ℓ_1 and j_1 correspond to the principal, orbital-angular-momentum and total-angular-momentum quantum numbers of the core electron, respectively. They indicate the ionization threshold to which the Rydberg series converges. The quantum numbers ℓ and j are associated to the angular momenta of the Rydberg electron, and J is the quantum number for the total angular momentum of the entire, two-electron system. We use below the notation $(N\ell_1 j_1 n\ell j)_J$ to denote the Rydberg states. Because the quantum defects δ_ℓ of the high- ℓ states considered in this work are very small, the difference between the principal quantum number n of the Rydberg electron and its effective principal quantum $\nu = n - \delta_\ell$ number is negligible in most cases. We thus use n interchangeably to describe either quantity. When channel interactions are strong, as is often the case for low ℓ values, the Rydberg series are strongly perturbed and mixed, such that the assignment to one single series is rather arbitrary.

Because the Hamiltonian matrix is complex-symmetric, its eigenvalues are complex and given by $E - i\Gamma/2$ (see Figs. 2(a) and 2(b) for the $\text{Sr}(5p_{1/2}ns_{1/2})_1$ and $\text{Ca}(4p_{1/2,3/2}np_j)_2$ series). When the eigenstates correspond to bound states and autoionizing resonances (red and blue solid circles), the eigenvalues are independent of the complex-rotation angle θ . The real part E gives the energy of the state while the imaginary part is half the autoionization rate Γ . The eigenvalues of continuum states, on the other hand, are rotated with respect to the real axis by $\sim 2\theta$ (gray solid circles).

To assess the accuracy and reliability of our calculations, we have compared the energies and autoionization rates of the calculated core-excited Rydberg states against available experimental data [44–50]. Overall, the agreement is excellent and the majority of the calculated rate agree with experimental data within the uncertainties.

Two examples are shown in Fig. 2 for the $\text{Sr}(5p_{1/2}ns_{1/2})_1$ series (panel a) and $\text{Ca}(4p_{1/2,3/2}np_j)_2$ series (panel b), confirming the excellent agreement over the entire range of n values measured in the experiments. In the upper figure, perturbations caused by the interaction of the $\text{Sr}(5p_{1/2}ns_{1/2})_1$ series with states belonging to series converging to the $\text{Sr}^+(5p_{3/2})$ threshold cause deviations from the smooth n^{-3} decrease of the autoionization rates with n [dashed line in Fig. 2(a)]. The positions of the perturber states, shown by the assignment bar within the figure, match the energies at which the autoionization rates of $(5p_{1/2}ns_{1/2})_1$ states are larger. This increase is caused by the mixing of these states with the perturber, which has a lower n value and therefore a larger autoionization rate. In the lower figure, similar perturbations occur but the larger number of Rydberg series involved makes the assignment of perturber states more complicated.

The CI-ECS approach thus allows the accurate calcu-

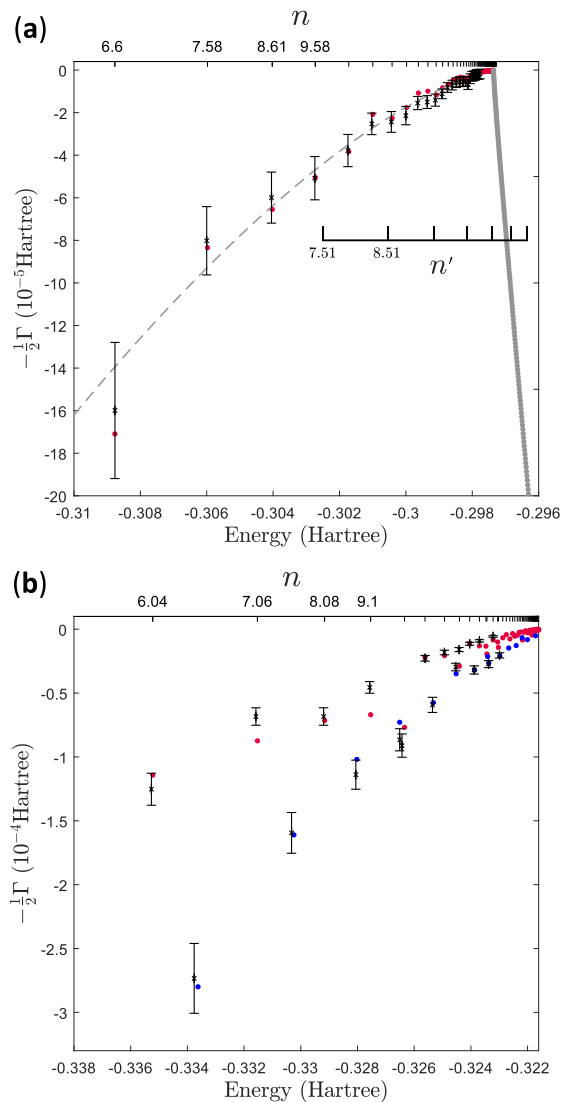


FIG. 2. Comparison between the energies and autoionization rates of core-excited Rydberg states calculated with CI-ECS and measured experimentally for (a) the $\text{Sr}(5p_{1/2}ns_{1/2})_1$ Rydberg series [44], and (b) the $\text{Ca}(4p_{1/2,3/2}np_j)_2$ series [45]. The red and blue solid circles in panel (b) represent $4p_{1/2}$ and $4p_{3/2}$ ion core states, respectively. The effective principal quantum numbers n relative to the $Np_{1/2}$ thresholds ($N = 4, 5$) are shown in the top horizontal axes. The assignment bar in panel (a) shows the effective principal quantum numbers n' of $\text{Sr}(5p_{3/2}ns_{1/2})_1$ states. The gray dashed line shows the overall n^{-3} scaling of autoionization rates.

lation of the energies and autoionization rates of core-excited Rydberg states, even in regions where perturbations between series are important. The extraction of the autoionization rates from the calculations is straightforward and does not involve fitting the density of states or the photoionization cross sections. It is ideally suited for large-scale calculations of autoionization rates.

B. Perturbation theory for high- ℓ states

Although in principle the autoionization rates can be calculated with CI-ECS for all values of ℓ , this approach becomes cumbersome at high ℓ where the rates reach values below the numerical accuracy of the calculations (typically 10^{-12} Hartree) and the numerical accuracy of double-precision arithmetics on the computer (10^{-16}). Whereas arbitrary-precision arithmetics could be used to reach higher accuracies, they make the calculation and diagonalization of the large complex-rotated Hamiltonian matrix very demanding computationally. For large ℓ values the centrifugal barrier experienced by the Rydberg electron is large and prevents its penetration in the ion-core region. The interelectronic distance r_{12} is always large and the electron repulsion is thus always small, such that a full treatment of two-electron correlations is no longer necessary. Instead, a perturbative treatment is possible which significantly simplifies the calculations and makes the use of arbitrary-precision arithmetics possible.

In the perturbative limit, a core-excited Rydberg state and its associated wavefunction are well described by a single jj -coupled configuration $(N\ell_1j_1n\ell_j)_J$,

$$|N\ell_1j_1n\ell_jJM_J\rangle = \sum_{\substack{m_{\ell_1} m_{\ell} \\ m_{s_1} m_s \\ m_{j_1} m_j}} \langle \ell_1 m_{\ell_1} \frac{1}{2} m_{s_1} | j_1 m_{j_1} \rangle \langle \ell m_{\ell} \frac{1}{2} m_s | j m_j \rangle \langle j_1 m_{j_1} j m_j | JM_J \rangle |N\ell_1 m_{\ell_1} \frac{1}{2} m_{s_1}\rangle |n\ell m_{\ell} \frac{1}{2} m_s\rangle, \quad (7)$$

with $|n\ell m_{\ell} \frac{1}{2} m_s\rangle$ and $|N\ell_1 m_{\ell_1} \frac{1}{2} m_{s_1}\rangle$ describing the spin-

orbitals of the Rydberg and core electrons, respectively.

We omitted antisymmetrisation in the above because, for high- ℓ states, the effect of exchange is negligible as the core and Rydberg electrons occupy very different regions of configuration space. The autoionization rate of a high- ℓ core-excited Rydberg state into a given continuum $(N'\ell'_1j'_1\varepsilon\ell'j')_J$ is given by Fermi's golden rule,

$$\Gamma = 2\pi \left| \langle N'\ell'_1j'_1\varepsilon\ell'j'JM_J | \frac{1}{r_{12}} | N\ell_1j_1n\ell_jJM_J \rangle \right|^2 \rho(\varepsilon), \quad (8)$$

with $\rho(\varepsilon)$ representing the continuum density of states at energy ε .

The matrix element in Eq. (8) is calculated by expanding the electron-electron repulsion $1/r_{12}$ in multipole terms [51]. Although there is a large number of terms in the expansion, we have observed that only the dipole ($q = 1$) and quadrupole ($q = 2$) terms contribute significantly to the calculated rates, *i.e.*, $\Gamma \simeq \Gamma^{(1)} + \Gamma^{(2)}$. For each multipole term $\Gamma^{(q)}$, carrying out the integration over all coordinates gives

$$\Gamma^{(q)} = 2\pi \left[R_{N\ell_1j_1}^{N'\ell'_1j'_1,q} R_{n\ell}^{\varepsilon\ell',q} \right]^2 |B^{(q)}|^2, \quad (9)$$

with the squared norm of the angular integral $B^{(q)}$ given by

$$\begin{aligned} |B^{(q)}|^2 &= [j_1, j'_1, j, j', \ell_1, \ell'_1, \ell, \ell'] \\ &\times \begin{pmatrix} \ell'_1 & q & \ell_1 \\ 0 & 0 & 0 \end{pmatrix}^2 \begin{pmatrix} \ell' & q & \ell \\ 0 & 0 & 0 \end{pmatrix}^2 \left\{ \begin{matrix} j_1 & q & j'_1 \\ \ell'_1 & 1/2 & \ell_1 \end{matrix} \right\}^2 \\ &\times \left\{ \begin{matrix} j & q & j' \\ \ell' & 1/2 & \ell \end{matrix} \right\}^2 \left\{ \begin{matrix} j' & j'_1 & J \\ j_1 & j & q \end{matrix} \right\}^2. \end{aligned} \quad (10)$$

with $k = \sqrt{2\varepsilon}$. The normalization constant $\mathcal{N}_{n,\ell}$ of the initial state is given by

$$\mathcal{N}_{n,\ell} = \frac{1}{(2\ell+1)!} \sqrt{\frac{(n+\ell)!}{(n-\ell-1)!2n}} \left(\frac{2}{n}\right)^{\ell+3/2} \quad (14)$$

and the one of the final state by

$$\mathcal{C}_{\varepsilon,\ell} = \frac{1}{(2\ell+1)!} \frac{2(2k)^\ell}{\sqrt{1 - \exp(-2\pi/k)}} \prod_{s=1}^{\ell} \sqrt{s^2 + \frac{1}{k^2}}. \quad (15)$$

The Appell F_2 function, along with all other functions in Eq. (13), can be calculated to within arbitrary numer-

We used the usual notation $[a, b, \dots] = (2a+1)(2b+1)\dots$

The radial integral

$$R_{N\ell_1j_1}^{N'\ell'_1j'_1,q} = \int dr_1 u_{N'\ell'_1j'_1}(r_1) r_1^q u_{N\ell_1j_1}(r_1) \quad (11)$$

involving the reduced radial wavefunctions $u_{n\ell_j}(r)$ of the core electron is calculated by considering that the influence of the distant Rydberg electron on the core electron is minimal, and that the core-electron radial wavefunction is identical to the one of the bare ion. The integral is then calculated using the ionic FEM-DVR basis functions obtained, as for the CI-ECS calculations, by solving the one-electron Schrödinger equation for the ion (see Sec. II A).

The radial integral for the Rydberg electron,

$$R_{n\ell}^{\varepsilon\ell',q} = \int dr_2 u_{\varepsilon\ell'}(r_2) r_2^{-q-1} u_{n\ell}(r_2), \quad (12)$$

is calculated using the fact that the Rydberg electron in a high- ℓ state experiences, to a very good approximation, the Coulomb potential of the singly charged ion core and nothing else. Because of the large centrifugal barrier, it does not penetrate into the core region where the electrostatic potential would depart from the Coulomb case. In other words, the quantum defect is vanishingly small (see [15] and [6] for details) and the Rydberg-electron radial wavefunction is hydrogenic. The integral is then known analytically in terms of the Appell hypergeometric function F_2 [52],

$$\begin{aligned} R_{n\ell}^{\varepsilon\ell',q} &= \mathcal{N}_{n,\ell} \mathcal{C}_{\varepsilon,\ell'} \Gamma(\ell + \ell' - q + 2) \left(\frac{1}{n} + ik\right)^{-(\ell+\ell'-q+2)} \\ &\times F_2(\ell + \ell' - q + 2, -\frac{1}{ik} + \ell' + 1, 2\ell + 2, 2\ell' + 2; \frac{2}{1+ikn}, \frac{2ikn}{1+ikn}), \end{aligned} \quad (13)$$

ical precision with the mpmath library [53]. For the calculations presented below, a numerical accuracy of 10^{-60} was chosen for the calculation of the radial integrals (13), which have values ranging from about 1 atomic unit at low ℓ to 10^{-50} atomic units at high ℓ . The other quantities entering Eq. (9) have values well above the numerical precision of the computer and can be calculated using double-precision arithmetics. The final result is obtained, using a numerical accuracy of 10^{-120} , by multiplying and squaring all quantities together to obtain $\Gamma^{(q)}$, by summing over the dipole and quadrupole contributions, and by summing over all continua accessible from the core-

excited Rydberg state under consideration. Because the squares of the angular integrals have values of typically 10^{-2} or larger, the relative numerical accuracy of the final results is guaranteed to be at least 10^{-10} for values up to 10^{-110} atomic units. This means that all the rates shown below, whose values reach as low as 10^{-100} , are calculated with sufficient numerical accuracy. Determining such minuscule autoionization rates is possible only with theoretical methods and not with experimental measurements, because the lifetimes involved are far too long and other decay mechanisms will dominate.

Anticipating on the results presented below, the rates calculated with the perturbative approach closely match the ones obtained by solving the full two-electron Schrödinger equation with CI-ECS for ℓ values in the range from 6 to 10 (see for example the blue and red circles in Fig. 3). Above $\ell \sim 10$, the rates are in general lower than the numerical accuracy of the CI-ECS calculations and only the perturbative approach provides reliable results. Below $\ell \sim 6$, perturbations are frequent. Because they cannot be represented within the single-configuration framework of the perturbative approach, only the CI-ECS method provides reliable results in this range. The agreement between the two methods in the $\ell \sim 6 - 10$ range validates the perturbative treatment for large ℓ values and shows that it is possible, when combining the two approaches, to accurately calculate the autoionization rates of core-excited Rydberg states over the *entire* range of possible ℓ values. The results provide benchmark data for future studies and, because they permit a systematic analysis of the role played by the Rydberg-electron angular momentum, they allow us to gain deep physical insight on the electronic dynamics responsible for autoionization.

III. RESULTS

We calculated the autoionization rates of all states of Mg, Ca, and Sr with $10 \leq n \leq 65$ and $0 \leq \ell \leq 45$ with the methods described above. The numerical results are provided in the Supplemental Material. In the following, we analyze the ℓ dependence of the rates and extract general behaviors from the large body of calculated data. In most cases, the rates decrease rapidly with ℓ , as expected from previous works [4, 16–21], but do not always follow a single decay trend. For $\ell \gtrsim 10$, the autoionization rates differ by several orders of magnitude depending on the values of j and J . For a given ion-core state and fixed values of $j - \ell$ and $J - \ell$, the evolution of the rates with ℓ is smooth and, anticipating on the results of Sec. IIID, follows simple scaling laws. We will see that this behavior is in fact governed by the value of $K - \ell$, with K the quantum number associated with the total angular momentum without Rydberg-electron spin. This allows us to define *branches* as ensembles of Rydberg states converging to a given ionization threshold and with fixed values of $K - \ell$, whose autoionization

rates behave in a similar manner. Such branches can exhibit a fine structure due to the spin-orbit interaction of the Rydberg electron. We first analyze the behavior of single branches, before considering all branches and later all thresholds of all species.

A. Behavior for a single branch

Figure 3 shows the autoionization rates of the $(4d_{5/2}45\ell_j)_J$ core-excited Rydberg states of Sr with $j = \ell - 1/2$ and $J = j + 1/2$ ($K - \ell = +\frac{1}{2}$). The calculated rates decrease by more than 20 orders of magnitude between $\ell = 1$ and $\ell = 44$. For $\ell \gtrsim 25$, they are far smaller ($\Gamma \lesssim 1 \text{ s}^{-1}$) than those of other decay mechanisms such as the fluorescence of the Rydberg electron, which takes place in the milliseconds range.

The decay of the rates in Fig 3 does not follow a single trend and a shoulder (shown by the arrow) is observed around $\ell = 7$. Its origin is, predominantly, the vastly different behavior of autoionization into the continua above the $\text{Sr}^+(5s_{1/2})$ and $\text{Sr}^+(4d_{3/2})$ ionization thresholds, both accessible from the $(4d_{5/2}45\ell_j)_J$ states (see Fig. 1). For the former threshold, the partial rates (empty gray circles) are large for small ℓ and fall very rapidly as ℓ increases. For the latter threshold, the partial rates (empty gray squares) are significantly smaller for small ℓ but decrease more slowly with ℓ and thus dominate the total autoionization rates for $\ell \gtrsim 10$.

Autoionization into the continua above both the $\text{Sr}^+(5s_{1/2})$ and $\text{Sr}^+(4d_{3/2})$ thresholds is predominantly caused by the quadrupolar part of the electron-electron repulsion. The kinetic energy of the emitted electron is however much larger for the $5s_{1/2}$ continua (1.84 eV) than for the $4d_{3/2}$ ones (0.035 eV). For large kinetic energies, the radial integral (13) for the Rydberg electron decreases much faster with ℓ than for smaller kinetic energies, a fact we verified in a systematic manner for electron kinetic energies from 0.3 eV to 8 eV and all possible values of ℓ . The other quantities entering the autoionization rates given by Eq. (9) vary only little or not at all with ℓ . Therefore, because of the Rydberg-electron radial integral, the rates decrease faster with ℓ for larger electron kinetic energies. We verified this property for the other series and thresholds of Sr, Ca and Mg. In conclusion, the shoulder in the rates of Fig 3 comes from the fact that two continua with very different energies are accessible upon autoionization.

Another shoulder can be observed for the partial rates into the continua above the $\text{Sr}^+(4d_{3/2})$ threshold (empty gray squares). In this case, it cannot be attributed to different photoelectron kinetic energies. Instead, it is explained by a change of the values of the angular integrals in Eq. (9) which finds its origin in the evolution of the angular-momentum coupling between the core and Rydberg electrons discussed in the following section.

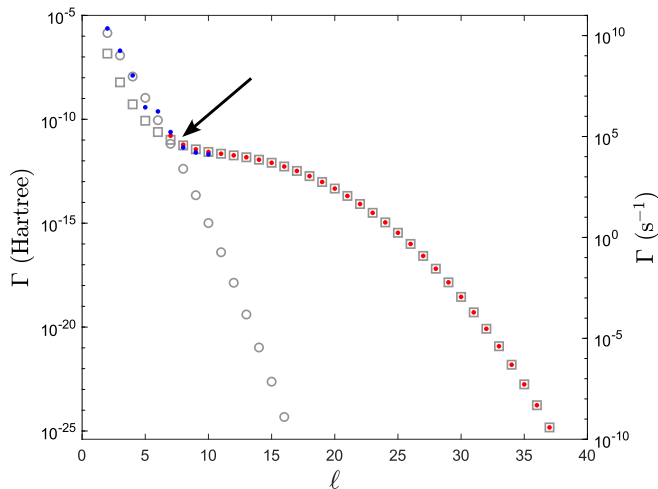


FIG. 3. Autoionization rates of the $(4d_{5/2}45\ell_j)_J$ core-excited Rydberg states of Sr as a function of the orbital quantum number of the Rydberg electron ($j = \ell - 1/2$ and $J = j + 1/2$). Solid blue circles represent the total rates calculated for low ℓ values with the CI-ECS method (Sec. II A) and red ones show the total rates calculated for large ℓ values with the perturbative approach of Sec. II B. The empty gray symbols show the partial decay rates to continua above the $5s_{1/2}$ (circles) and $4d_{3/2}$ (squares) ionization thresholds calculated with the perturbative approach.

B. Behavior for all branches

We now consider the behavior of autoionization rates with ℓ for all possible values of j ($\ell \pm \frac{1}{2}$) and J ($j + j_1 \geq J \geq |j - j_1|$). The value of n is fixed and we consider a single ionization threshold (N, ℓ_1, j_1 fixed). Figure 4 shows the rates of the $(5p_{3/2}45\ell_j)_J$ states of Sr. At low ℓ values, the Rydberg electron penetrates into the ion core region. Its wave function significantly overlaps with the one of the core electron and the quantum defects are large. Perturbations between adjacent Rydberg series are frequent (see Fig 2(b) for example) and the autoionization rates do not exhibit a regular behavior for $\ell \lesssim 4$ (region I in Fig. 4). In an intermediate region between $\ell \sim 4$ and $\ell \sim 8$ (region II), the rates decrease monotonically and their magnitudes are similar for all values of j and J . In the last region (region III), they split into what appears to be three branches with very different magnitudes but similar evolution with ℓ . The apparent branches are further split by the spin-orbit interaction of the Rydberg electron, leading to two fine-structure components with slightly different rates (solid circles and crosses in Fig 4).

The branches can be associated to different values of $K - \ell$, K being the quantum number of the total angular momentum excluding Rydberg-electron spin. This is not surprising because, when the spin-orbit interaction of the Rydberg electron is negligible, intermediate (jK) coupling is the most appropriate coupling scheme for core-excited Rydberg states [6]. The total angular momentum j_1 of the core electron strongly couples to

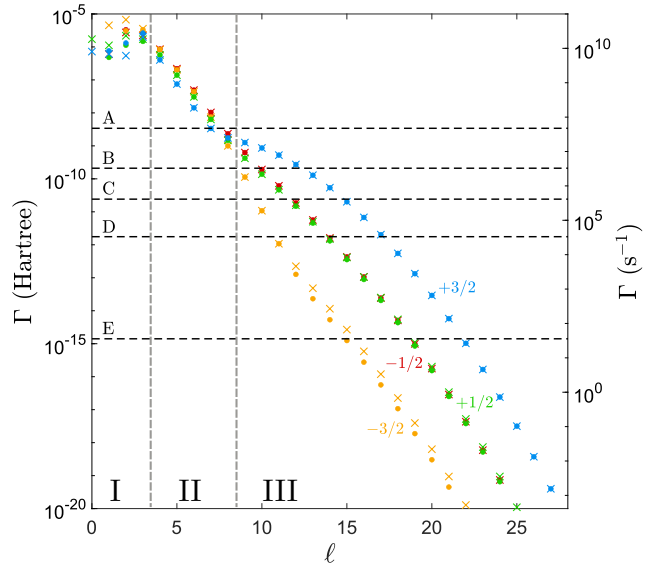


FIG. 4. Autoionization rates of the $(5p_{3/2}45\ell_j)_J$ states of Sr as a function of ℓ for all possible j and J values. The different branches are labeled, and their color is chosen, according to the value of $K - \ell$ (see text). Each branch has a fine structure corresponding to the fine structure of the Rydberg electron. The two fine-structure components are associated with the two possible values of the coupling between K and the spin of the Rydberg electron (solid circles for $J = K - \frac{1}{2}$ and crosses for $K + \frac{1}{2}$). The horizontal dashed lines labeled A, B, C, D and E represent the decay rates of the radiative deexcitation channels $5p_{3/2} \rightarrow 5s_{1/2}$, $5p_{3/2} \rightarrow 4d_{5/2}$, $5p_{3/2} \rightarrow 4d_{3/2}$, $5s45p \rightarrow 5s^2$ and $45c \rightarrow 44c$, respectively, with c representing circular Rydberg states.

the orbital angular momentum ℓ of the Rydberg electron to give K . The jj -coupled states that we calculate with the methods of Sec. II are related to intermediate-coupling states by the transformation coefficients [51]

$$|N\ell_1 j_1 n \ell j J\rangle = \sum_K (-1)^{j_1 + \ell + \frac{1}{2} + J} \sqrt{(2K+1)(2j+1)} \begin{Bmatrix} j_1 & \ell & K \\ \frac{1}{2} & J & j \end{Bmatrix} |N\ell_1 j_1 n \ell K J\rangle. \quad (16)$$

For large ℓ values, there is an almost one-to-one correspondence between a given jK -coupled state, which we denote as $(N\ell_1 j_1 n \ell)_K$ below, and the two jj -coupled $(N\ell_1 j_1 n \ell_{j=\ell \pm 1/2})_{J=K \pm 1/2}$ states, thus making the assignment straightforward.

For the rates shown in Fig. 4, there are four possible values of K for each value of ℓ ($K - \ell = \pm \frac{1}{2}, \pm \frac{3}{2}$). The four corresponding branches are distinguished by their color and labelled by their $K - \ell$ value. The spin-orbit interaction of the Rydberg electron further splits the $K - \ell$ branches into two sub-branches with $J = K + 1/2$ and $J = K - 1/2$ (crosses and solid circles in Fig. 4, respectively). This effect is very small, as expected because the

spin-orbit interaction of the Rydberg electron is small, and it is in fact only visible for the $K - \ell = -3/2$ branch (orange crosses and circles).

The very different magnitudes of the autoionization rates of the branches trace back to the interplay between the radial and angular parts of the electron-electron repulsion in Eq. (9). For $\ell \gtrsim 10$, autoionization into the continua above the $5p_{1/2}$ threshold dominates over autoionization into those above the $4d_{3/2,5/2}$ and $5s_{1/2}$ thresholds because the photoelectron kinetic energy is much smaller in the former case (see Fig. 1). The $(5p_{3/2}45\ell_j)_J$ states couple to the $5p_{1/2}$ continua through the quadrupolar (tensor order of 2) part of the electron-electron repulsion ($q = 2$). Upon autoionization, ℓ is thus unchanged or changes by 2 ($\Delta\ell = \ell' - \ell = 0, \pm 2$). Importantly, the radial integrals $\langle \varepsilon \ell' | 1/r_2^3 | n\ell \rangle$ differ by several orders of magnitude depending on the value of $\Delta\ell$, with $\Delta\ell = +2$ being the largest [see Fig. 6(a)]. The same observation applies for the dipole (tensor order of 1) part of the electron repulsion ($q = 1$), in which case the radial integrals are much larger for $\Delta\ell = +1$ than for $\Delta\ell = -1$. A similar situation is encountered for the dipole matrix elements describing photoabsorption and photoionization in hydrogenic systems, for which $\Delta\ell = +1$ transitions dominate over $\Delta\ell = -1$ transitions [54].

Because K (or J for jj coupling) must be conserved upon autoionization, angular-momentum coupling constrains the possible changes of ℓ for a given branch. Considering the quadrupolar interaction, the initial state $(5p_{3/2}n\ell)_{K=\ell-3/2}$ can only autoionize into continua above the $5p_{1/2}$ threshold with $\ell' = \ell - 2$. Continua with $\ell' = \ell + 0, 2$ are inaccessible because in these cases angular-momentum coupling between the $5p_{1/2}$ core electron and the ℓ' ionized electron cannot yield $K = \ell - 3/2$ and K cannot be conserved. The autoionization of the states of the $-3/2$ branch thus involves a $\Delta\ell = -2$ transition only, with a small radial integral translating into small values for the rates (orange crosses and circles in Fig. 4). The opposite observation holds for the $K - \ell = +3/2$ branch. Only the $\Delta\ell = +2$ transition is possible and, because the corresponding radial integral is large, the autoionization rate is large (blue crosses and circles in Fig. 4). For the $K - \ell = \pm 1/2$ branches (red and green circles and crosses in Fig. 4), the only possible transition is $\Delta\ell = 0$, which explains why the rates of both branches are very similar and lie between those of the $+3/2$ ($\Delta\ell = +2$) and $-3/2$ ($\Delta\ell = -2$) branches.

The above analysis revealed that the gross structure of the branches is related to which $\Delta\ell$ value contributes predominantly to autoionization. Let us consider another example, the $4d_{5/2}n\ell$ states of Sr, which for large ℓ values autoionize predominantly into continuum above the $\text{Sr}^+(4d_{3/2})$ threshold through quadrupole interactions. As illustrated in Fig. 5, six branches ($K - \ell = \pm\frac{1}{2}, \pm\frac{3}{2}$ and $\pm\frac{5}{2}$) can be observed which are grouped into 3 main components. The lowest branch and component, which is further split by the spin-orbit interaction of the Rydberg electron, is $K - \ell = -5/2$ and autoionizes through

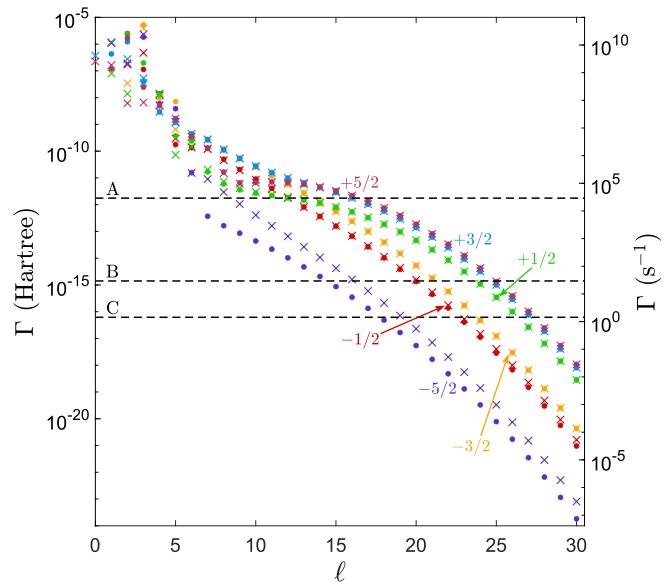


FIG. 5. Autoionization rates of the $(4d_{5/2}45\ell_j)_J$ states of Sr as a function of ℓ for all possible j and J values. The symbols and colors are defined as in Fig. 4. The horizontal dashed lines labeled A, B and C represent the decay rates of the radiative deexcitation channels $5s45p \rightarrow 5s^2$, $45c \rightarrow 44c$, and $4d_{5/2} \rightarrow 5s_{1/2}$, respectively, with c representing circular Rydberg states.

$\Delta\ell = -2$ transitions only. The intermediate branches $K - \ell = -3/2$ and $-1/2$ autoionize through predominantly $\Delta\ell = 0$ transitions, and the branches with the largest rates, $K - \ell = 1/2, 3/2$ and $5/2$ autoionize through strong $\Delta\ell = +2$ transitions. The substructure within the three main $\Delta\ell$ components is due to differences in angular-momentum coupling which translate into different values of the angular integrals in Eq. (9).

The conclusions drawn above implicitly rely on the assumption that the angular integrals entering the autoionization rates have similar magnitudes for any $\Delta\ell$. As shown in Fig. 6 this is verified for large ℓ ($\ell \gtrsim 10$) and thus K values. The underlying reason can be made explicit by considering the large- ℓ behavior of the angular integrals. We use jK coupling to make the behavior more apparent, however similar conclusion can be drawn with jj coupling as well. As shown in appendix A, the asymptotic formulas for the Wigner symbols [55] allow to reduce the norm squared of the angular integral $B^{(q)}$ in jK coupling to

$$\begin{aligned} |B^{(q)}|^2 &\sim [\ell_1, \ell'_1, j_1] \begin{pmatrix} \ell'_1 & q & \ell_1 \\ 0 & 0 & 0 \end{pmatrix}^2 \left\{ \begin{matrix} j_1 & q & j'_1 \\ \ell'_1 & 1/2 & \ell_1 \end{matrix} \right\}^2 \\ &\times \left[D_{0\Delta\ell}^q(0, \frac{\pi}{2}, 0) \right]^2 \\ &\times \langle j_1(K - \ell)q(-\Delta\ell) | j'_1(K - \ell - \Delta\ell) \rangle^2, \quad (17) \end{aligned}$$

where D is the Wigner rotation matrix. Importantly,

the integral no longer depends on the values of ℓ and K but only on their difference $K - \ell$, *i.e.*, on the branch under consideration. They also depend on $\Delta\ell$ which, for a given branch, can be taken as the largest value allowed by angular-momentum coupling because it corresponds to the largest radial integral.

Equation (17) describes the change of angular momentum of the core electron ($j_1 \rightarrow j'_1$) through its q -pole coupling with the Rydberg electron. It is particularly instructive because, when multiplied by the radial integrals (see Eq. (A5)), it describes an electric dipole ($q = 1$) or electric quadrupole ($q = 2$) optical transition of the core electron,

$$\Gamma^{(q)} \sim 2\pi \left[R_{n\ell}^{\varepsilon\ell',q} D_{0\Delta\ell}^q(0, \frac{\pi}{2}, 0) \right]^2 \times |\langle N\ell_1 j_1(K-\ell) | r_1^q C_{q,-\Delta\ell} | N'\ell'_1 j'_1(K-\ell-\Delta\ell) \rangle|^2 \quad (18)$$

with an effective “light” intensity given by the two terms between the square brackets on the right hand side. $C_{q,-\Delta\ell}(\theta_1, \phi_1)$ is an unnormalized spherical harmonic.

The transition dipole or quadrupole moment of the core electron in equation (18) involves the projection of the core-electron angular momentum \mathbf{j}_1 onto an axis that is no longer the quantization axis but, rather, another axis defined by the electron repulsion. The same coefficient also shows that the projection of \mathbf{j}_1 onto the new axis is $K - \ell$. We have shown earlier that the different branches correspond to different $K - \ell$ values. We can therefore relate the branches to the orientation of the core-electron angular momentum relative to the axis defined by its coupling to the Rydberg electron. Like the branch, this orientation has a crucial influence on the autoionization of high- ℓ core-excited Rydberg states.

For lower values of ℓ , the angular integrals rapidly change with ℓ (see Fig. 6), and their magnitudes differ significantly. Transitions that change K become non-negligible (gray lines in Fig. 6). The relative magnitude of the autoionization rates in different branches can no longer be simply estimated, and we have observed in all our calculations that the rates become in fact similar regardless of the branch for values below $\ell \lesssim 10$.

C. General behavior for alkaline-earth species

In addition to Sr, we also calculated the autoionization rates of core-excited Rydberg states of Mg and Ca. The ionization thresholds $Np_{1/2}$, $Np_{3/2}$ and, when applicable, $(N-1)d_{3/2}$ and $(N-1)d_{5/2}$, were considered ($N = 3 - 5$, see Fig. 1). The rates of the three species evolve in a similar way with ℓ , as illustrated by the examples shown in Fig. 7. The similarity is not surprising as all alkaline-earth-metal ions possess the same electronic structure, with the exception of the $(N-1)d_{3/2,5/2}$ states only present for Ca and the heavier species. For high ℓ values the Rydberg electron is essentially hydrogenic regardless of the atomic species. Differences in the values

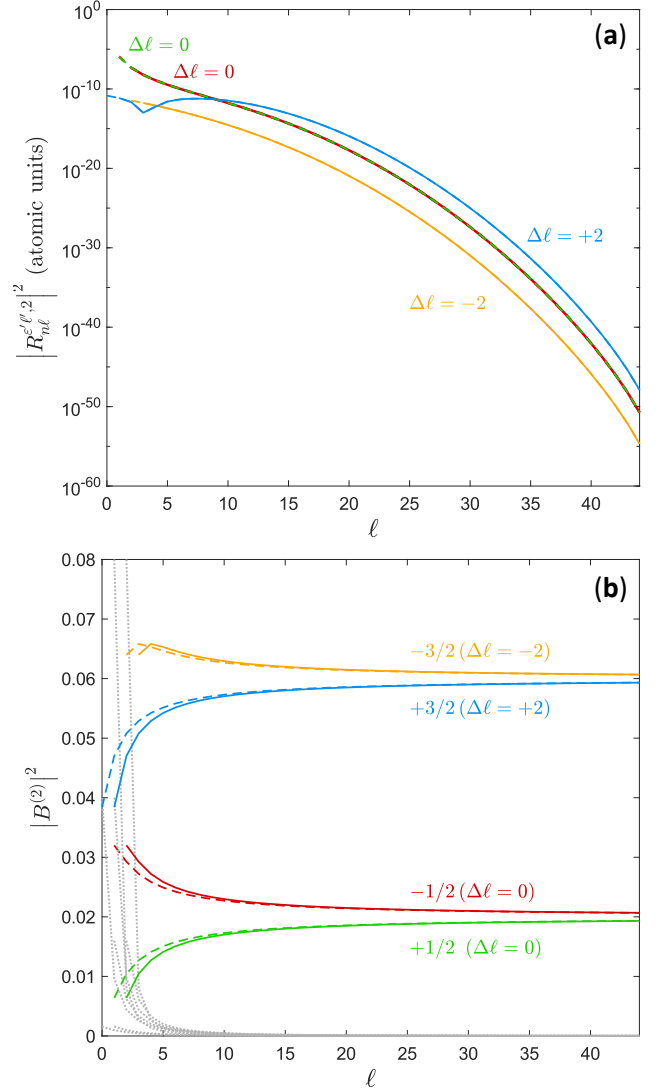


FIG. 6. ℓ dependence of the norm squared of (a) the radial integrals for the Rydberg electron (13) and (b) the angular integrals (10) for $\text{Sr}(5p_{3/2}45\ell_j)_J$ states with all possible j and J values. Orange, red, green and blue lines correspond to $K - \ell = -3/2, -1/2, +1/2$ and $+3/2$ branches, respectively. The solid and dashed lines for the angular integrals represent the two possible couplings of the Rydberg-electron spin with K ($J = K - 1/2$ and $+1/2$, respectively). The gray lines are angular integrals for which J is conserved but not K . For the colored lines, both J and K are conserved

of the rates are thus due to the different properties of the ion cores, in particular the energies of the states, which affect the photoelectron kinetic energies, and the transition dipole moment $\langle N'\ell'_1 j'_1 | r_1 | N\ell_1 j_1 \rangle$ and transition quadrupole moment $\langle N'\ell'_1 j'_1 | r_1^2 | N\ell_1 j_1 \rangle$, which directly enter the calculation of the autoionization rates.

For the series converging to the $Np_{1/2}$ thresholds [Fig. 7(a)], the continua above the $Ns_{1/2}$ threshold and, except for Mg, the $(N-1)d_{3/2}$ threshold are accessible.

The latter dominate at high ℓ values, a fact we verified by calculating the partial rates. The influence of the photoelectron kinetic energy on the speed at which the rates decrease is conspicuous. Indeed, the energy difference between the $3s_{1/2}$ and $3p_{1/2}$ thresholds in Mg (4.422 eV) is much larger than the one between the $3d_{3/2}$ and $4p_{1/2}$ thresholds in Ca (1.431 eV) or the $4d_{3/2}$ and $5p_{1/2}$ thresholds in Sr (1.136 eV), and the rates for Mg decay much faster than for the other two species. We observe that, as before, the faster the photoelectron the faster the rates decrease with ℓ .

The rates of series converging to the $Np_{3/2}$ thresholds of Mg, Ca, Sr, and belonging to the branch with $K - \ell = +\frac{1}{2}$, are shown in Fig. 7(b). Autoionization proceeds in the continua above the $Ns_{1/2}$, $Np_{1/2}$ and, for Ca and Sr, the $(N - 1)d_{3/2,5/2}$ ionization thresholds. At low ℓ values, the dipole-type coupling to the $Ns_{1/2}$ and $(N - 1)d_{5/2}$ continua and the quadrupole-type coupling to the $(N - 1)d_{3/2}$ continua are all important. We observe, as in Fig. 3 and 4, a change in the decay trend around $\ell \sim 10$ after which autoionization to continua above the $Np_{1/2}$ threshold is the major decay channel. The same observations as for Fig. 7(a) can be made regarding the relationship between the photoelectron kinetic energy and the speed at which the rates decrease with ℓ . The spin-orbit splitting of the $\text{Mg}^+(3p_{1/2,3/2})$ levels (11.4 meV) is the smallest of the three species and the rates are the largest for large ℓ . The rates for Mg decrease by only 5 orders of magnitude in the range from $\ell = 10$ to $\ell = 30$, whereas those of Ca and Sr decrease by 9 and 16 orders of magnitude, respectively. The reasoning holds for all other branches and all other thresholds of the three species we investigated.

D. Comparison against available high- ℓ experimental data

Quantitative experimental data on the autoionization rates of high- ℓ core-excited Rydberg states are scarce even for the alkaline-earth-metal atoms which, in comparison, have been extensively studied for low ℓ values (see Ref. 6 for a review). Cooke *et al.* [4] measured the autoionization rates of $(5p_{j_1}n\ell_j)_J$ states of Sr for $n = 16$ and $\ell = 3 - 5$. Their data, shown in Fig. 8, falls in good agreement with our CI-ECS results (black crosses and red solid circles, respectively). In the experiment, the autoionization rates were determined from the overall linewidths of $5p_{j_1}n\ell$ states, their j and J substructure being unresolved. For a given ℓ value, the experimental linewidth is therefore the result of both the combined autoionization linewidths of all j and J sublevels, and the small energy differences between these sublevels. We modeled this with our CI-ECS data by generating Lorentzian line profiles for each sublevel, with center frequencies and linewidths given by the results of the calculations. These profiles were then summed and the overall linewidths determined in a least-square fit to a Lorentzian

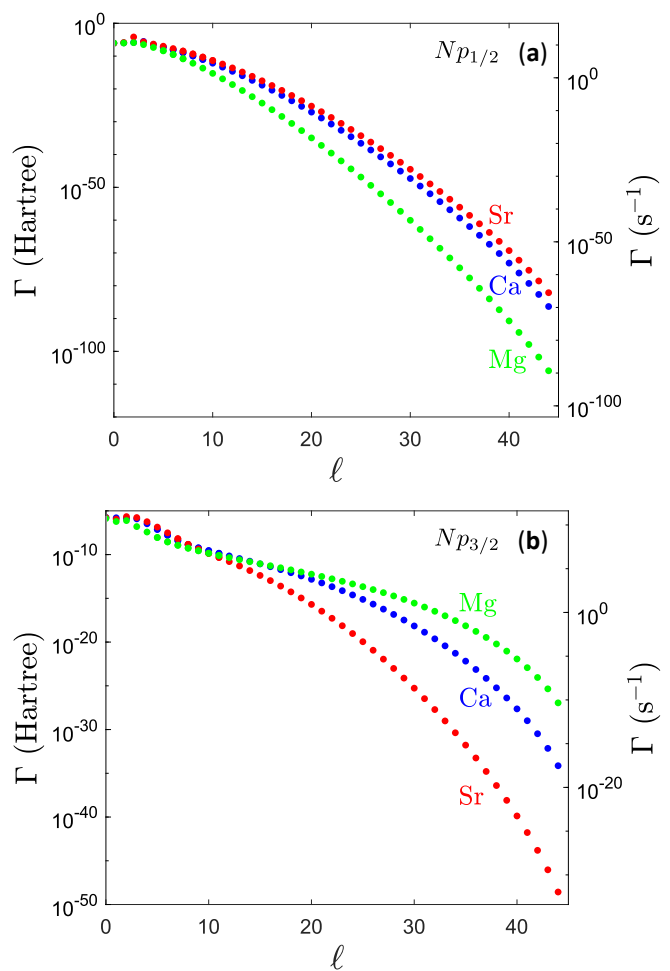


FIG. 7. (a) Autoionization rates of the $(Np_{1/2}45\ell_j)_J$ states of Mg (solid green circles), Ca (solid blue circles) and Sr (solid red circles) as a function of ℓ for the $K - \ell = 1/2$ branch ($j = \ell + 1/2$ and $J = j + 1/2$). (b) Same as panel (a) for the $Np_{3/2}$ thresholds.

function. It is these values that are shown in Fig. 8 (red solid circles).

The $(4d_{3/2,5/2}51c_j)_J$ circular core-excited Rydberg states of Sr, i.e, those of maximal orbital and magnetic quantum numbers of the Rydberg electron $|m| = \ell = n - 1$, have been shown to be stable against autoionization by Teixeira *et al.* [18]. They could experimentally determine lower bounds for the autoionization lifetimes of $\text{Sr}(4d_{3/2}51c)$ and $\text{Sr}(4d_{5/2}51c)$ circular states of 5 ms and 2 ms, respectively. Our calculations agree with these lower bounds and in fact predict lifetimes that are longer by many orders of magnitude (77 and 21, respectively). We can thus confirm that circular core-excited Rydberg states are completely immune to autoionization. Our results reveal that, in fact, most states with $\ell \geq 22$ are also immune to autoionization, in the sense that autoionization lifetimes are longer than even the fluorescence lifetime of the Rydberg electron (millisecond range).

In a recent work, Yoshida *et al.* [13] thoroughly investi-

gated the autoionization of the $5p_{1/2}n\ell$ states of Sr with $\ell = 0 - 5$. To compare our CI-ECS results with the data presented in [13], we determined the scaled autoionization rates Γ_0 of the $(5p_{1/2}n\ell_j)_J$ series ($\ell = 3 - 5$) by fitting the calculated rates to the usual formula

$$\Gamma(n) = \frac{\Gamma_0}{n^3} \quad (19)$$

in the range $n = 51 - 75$. The scaled rates are compared in Table IV and show good agreement with the results of [13]. For lower ℓ values, the rates do not closely follow the scaling law (19) because of series perturbations.

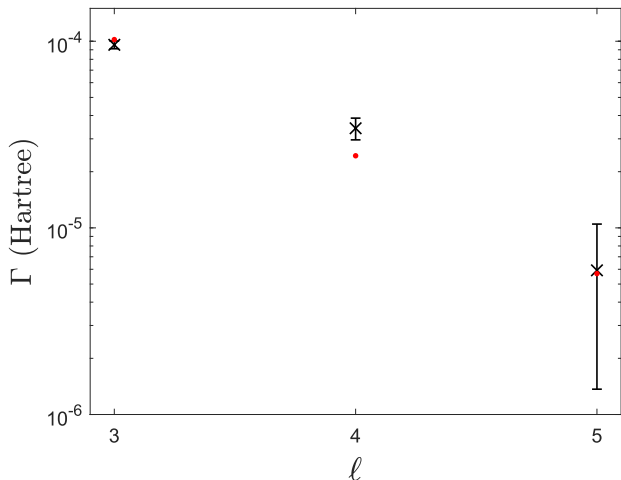


FIG. 8. Autoionization rates of the $(5p_{1/2}16\ell)$ states of Sr obtained experimentally (black crosses, [4]) and theoretically (red solid circles, present results). The values shown here are the combined rates for all the sublevels with same ℓ but different j and J values (see text).

E. ℓ and n scaling

Beyond $\ell \sim 4$ Rydberg-series perturbations are rare and the behavior of the autoionization rates with ℓ is smooth. We found that the decrease of the rates with ℓ is well described by the empirical exponential law

$$\Gamma(\ell) = \Gamma_0 e^{a\ell^2 + b\ell}, \quad (20)$$

where Γ_0 , a and b are parameters that depend on n and on the branch under consideration. They can be determined in a least-squares fit of the calculated rates ($\ell = 5 - 30$) yielding, for example, $\Gamma_0 = 3.5(15) \cdot 10^{-4}$ Hartree, $a = -0.064(2)$ and $b = -2.69(6)$ for the $(3p_{1/2}45\ell_{\ell-1/2})_{j-1/2}$ series of Mg. The law is shown by the solid black line in Fig. 9 and compared against the calculated data (red crosses). It reproduces the rates to within 30% or better over the 60 orders of magnitude that their values span. Increasing the degree of the polynomial in the exponential leads to a more accurate fit, at

TABLE IV. Comparison between the experimental and theoretical scaled autoionization rates Γ_0 from Ref. [13] and the present theoretical values for the $(5p_{1/2}n\ell_j)_J$ Rydberg series of Sr ($\ell = 3 - 5$). In the experiment [13], the rates of Rydberg series with the same ℓ values but different j and J values could not be individually determined.

Series	Γ_0^{exp} [13]	Γ_0^{th} [13]	Γ_0^{th} (present)
$(5p_{1/2}nf_{5/2})_{J=2}$	0.181	0.199	0.234
$(5p_{1/2}nf_{5/2})_{J=3}$		0.164	0.165
$(5p_{1/2}nf_{7/2})_{J=3}$		0.201	0.207
$(5p_{1/2}nf_{7/2})_{J=4}$		0.230	0.194
$(5p_{1/2}ng_{7/2})_{J=3}$	0.056	0.081	0.069
$(5p_{1/2}ng_{7/2})_{J=4}$		0.046	0.042
$(5p_{1/2}ng_{9/2})_{J=4}$		0.081	0.069
$(5p_{1/2}ng_{9/2})_{J=5}$		0.046	0.042
$(5p_{1/2}nh_{9/2})_{J=4}$	0.027	0.015	0.018
$(5p_{1/2}nh_{9/2})_{J=5}$		0.006	0.009
$(5p_{1/2}nh_{11/2})_{J=5}$		0.015	0.018
$(5p_{1/2}nh_{11/2})_{J=6}$		0.006	0.010

the expense of an increased number of parameters. We find that a second order polynomial represents a good compromise between accuracy and simplicity.

Equation (20) describes the rates well when a single decay trend is observable. When the rates show several decay trends, typically associated with autoionization into the continua of different ion-core states, the behavior is well described by the sum of exponential laws

$$\Gamma(\ell) = \sum_{i=1}^k \Gamma_0^{(i)} e^{\alpha^{(i)}\ell^2 + b^{(i)}\ell} \quad (21)$$

k is typically the number of ion-core thresholds with significantly different energies. The rate values obtained by fitting the above equation, choosing $k = 2$, to the theoretical results for the $\text{Ca}(4p_{3/2}45\ell_{\ell+1/2})_{\ell+2}$ branch ($\ell = 5 - 30$) are shown in Figure 10. As for the single-trend case, the agreement between the fit results and the calculated values is excellent and better than 20% over the entire range ($\ell = 5 - 30$).

An approximate formula for the ℓ dependence of autoionization rates, derived in Ref. [56], predicts a polynomial dependence $\Gamma \propto 1/n^3 \ell^{4q-3}$ where q is the order of the multipole expansion giving the dominant contribution to autoionization. The prediction has been verified for the low ℓ states of the $\text{Sr}(5p_{1/2}n\ell)$ series [13] ($\ell \lesssim 5$) but, as ℓ increases, it rapidly deviates from our results. The same is true for other series and species and, in the case of Mg shown in Fig. 9 (dashed gray line), the deviation occurs at even smaller ℓ values. The deviation can be attributed to the assumptions made in Ref. [56] to analytically estimate the radial integral (13) and the rate (8), leading to the polynomial scaling, whereas the integral is calculated exactly in the present work.

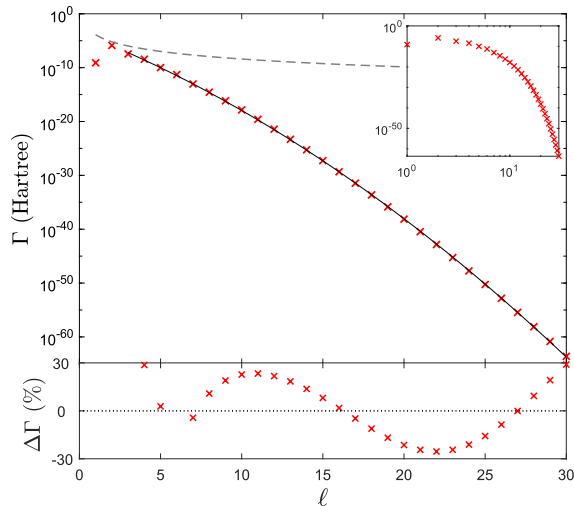


FIG. 9. Calculated autoionization rates (red crosses) of the $(3p_{1/2}45\ell_j)_J$ states of Mg for the $K-\ell = -\frac{1}{2}$ branch ($j = \ell - \frac{1}{2}$ and $J = j - \frac{1}{2}$). Formula (20) is shown by the black solid line, with parameters obtained in a least-squares fit of the calculated data in the range $\ell = 5 - 30$. The gray dashed line corresponds to the polynomial scaling discussed in text. The inset shows the same values on a log-log scale, highlighting the absence of polynomial scaling of the rates with ℓ . The bottom part of the graph shows the fit residuals on a relative scale.

The n^{-3} scaling of autoionization rates is well established for low ℓ values but deserves a closer inspection as ℓ increases. When $n \gg \ell$, the cubic scaling is verified [15] as illustrated in Fig. 11(a) for the $(4p_{3/2}n(\ell = 7)_{15/2})_7$ series of Ca. Clear deviations appear when n becomes comparable to ℓ , as shown in Fig. 11(b) for the same branch but a higher $\ell = 18$ value. In this situation, the rates initially increase with n before passing through a maximum and eventually following the expected n^{-3} asymptotic form (blue dashed line) as $n \gg \ell$. The same observation holds for all other branches, ion-core states, and atomic species that we studied.

A departure from the n^{-3} scaling law is well known for the fluorescence lifetimes of high- ℓ Rydberg states. In this case, because the fluorescence only occurs to nearby states of similar n values, a scaling of n^{-5} can be derived [15]. Autoionization proceeds, instead, to continua with the same energy regardless of the value of ℓ and, therefore, an argument similar to the one for fluorescence cannot be made. The n dependence of the autoionization rates, encoded in the complicated functions shown in Eq. (13), depends on the kinetic energy of the ionized electron and does not follow a simple polynomial scaling law.

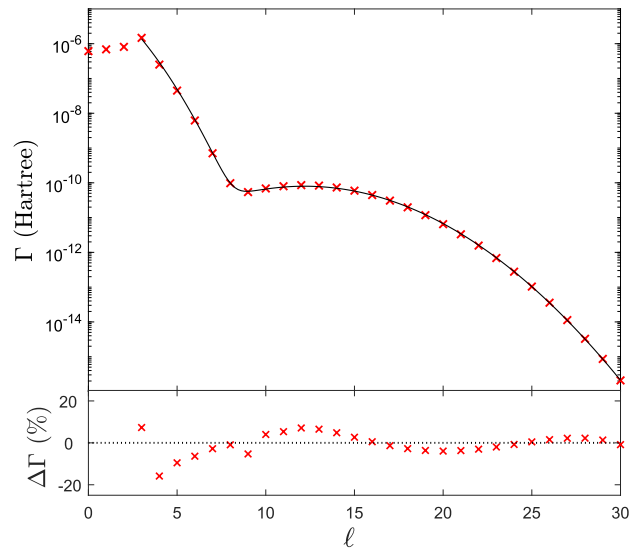


FIG. 10. Calculated autoionization rates of the $\text{Ca}(4p_{3/2}45\ell_j)_J$ series with $j = \ell + 0.5$ and $J = j + 1.5$ (red crosses). The solid line shows formula (21) with $k = 2$ and parameters obtained in a least-squares fit of the calculated data in the range $\ell = 5 - 30$. The bottom part of the graph shows the fit residuals on a relative scale.

IV. CONCLUSION

The autoionization rates of core-excited states of Mg, Ca and Sr were calculated for $n = 10 - 65$ and $\ell = 0 - 45$. For low ℓ values, we obtained the rates by treating the full extent of correlations between the two valence electrons with CI-ECS. Both the values of the rates and the perturbations caused by states belonging to other, adjacent Rydberg series fall in excellent agreement with the available experimental data. Beyond $\ell \sim 5$, the rates drop rapidly and perturbations become much scarcer, two facts indicating the rapid decrease of the electron-electron repulsion. We show that a perturbative treatment of dipole- and quadrupole-type electron correlations, which compares well to the results of the full nonperturbative CI-ECS calculations, is sufficient at this point. The hydrogenic integrals involved in the perturbative calculations are computed without approximation and with a numerical precision of 10^{-60} , a fact imposed by the rapid decrease of the rates with ℓ .

The complete picture provided by the results has allowed us to analyze the autoionization of high- ℓ core-excited Rydberg states in detail and derive both the quantum number dependencies of their autoionization dynamics and the physical mechanisms responsible for these dependencies. Five general laws have been identified:

First, the decay of the autoionization rates with ℓ is very rapid. Above $\ell \sim 25$, they become negligible compared to all other decay processes, even those as slow as

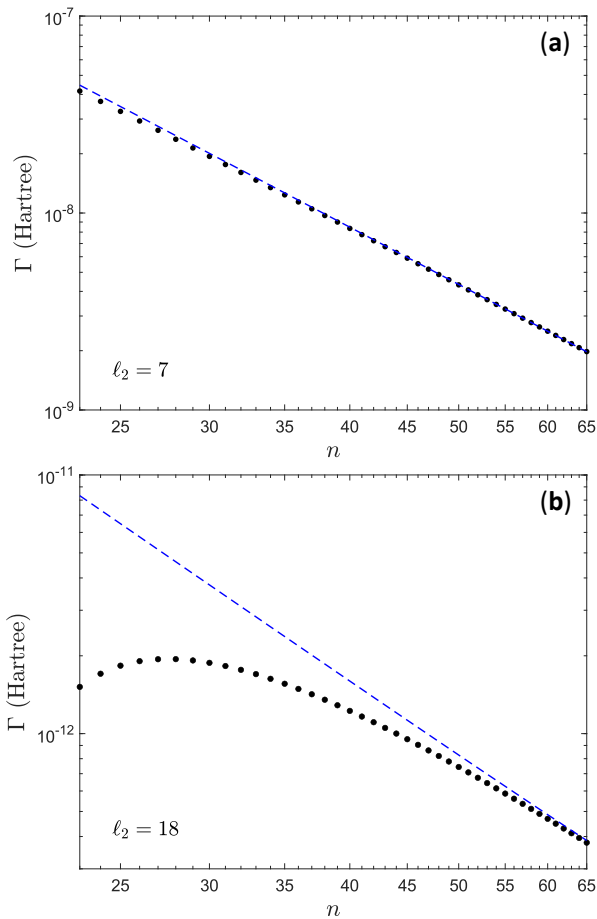


FIG. 11. Dependence of the calculated autoionization rates on n for the $(4p_{3/2}n\ell_j)_J$ Rydberg series of Ca with (a) $\ell = 7$, and (b) $\ell = 18$. In both cases we chose $j = \ell + 1/2$ and $J = j - 1/2$. The blue dashed line represents the n^{-3} scaling law reached when $n \gg \ell$. For $n < 23$, autoionization into the continua above the $\text{Ca}^+(4p_{1/2})$ threshold is no longer energetically allowed and the rates are much smaller.

the fluorescence of the Rydberg electron taking place on the millisecond timescale.

Second, the values of the rates separate into branches belonging to different $K - \ell$ values, *i.e.*, different couplings between the total angular momentum of the ion core and the orbital angular momentum of the Rydberg electron. Each branch can be associated to predominantly one change of ℓ upon autoionization ($\Delta\ell = \pm 1$ for $q = 1$ and $\Delta\ell = 0, \pm 2$ for $q = 2$), a property resembling selection rules in radiative transitions. Depending on the predominant $\Delta\ell$, the values of the rates differ by up to several orders of magnitude which gives rise to well separated branches.

Third, for each branch the decrease of the rates with ℓ presents a single decay trend if autoionization proceeds predominantly into the continua above a single ion-core state. Otherwise, several decay trends can be observed. The speed at which the rates decrease is determined by

the energy of the autoionized electron, therefore the different trends are particularly pronounced when autoionization occurs into continua above ion-core states that have very different energies. In that case, a shoulder is observed around $\ell \sim 8$ where the rapid decrease of the rates suddenly turns into a much slower one. A similar trend has been observed in other species such as the Yb atom [17].

Fourth, autoionization rates are typically larger when the kinetic energy of the electron is small, and smaller when this energy is large. This means, for example, that the rates for the $\text{Mg}(3p_{1/2}n\ell)$ series are smaller than those of the $\text{Ca}(4p_{1/2}n\ell)$ and $\text{Sr}(5p_{1/2}n\ell)$ series because the $\text{Mg}^+(3p_{1/2})$ ion-core state lies the highest in energy.

Fifth, the autoionization rates decrease with ℓ following, to a good approximation, an exponential law in which the argument is a second-order polynomial in ℓ . Using this law the rates can be described within a good relative accuracy over the many orders of magnitude that they span. This scaling law can be used, in the future, to extrapolate the rates from a small set of measured high- ℓ autoionization rates to other ℓ values. The dependence of the rates on n follows the usual n^{-3} scaling law when $n \gg \ell$. This is no longer the case when n and ℓ are similar, in which case no simple scaling law has been found.

The general laws presented above were derived from the extensive data calculated for the alkaline-earth-metal atoms. For high- ℓ states, the exact shape of the ion core has only little influence on the Rydberg electron as, because of the centrifugal barrier, it does not penetrate in the ion core region. The conclusions drawn above are therefore not limited to alkaline-earth-metal species and are expected to apply to high- ℓ Rydberg states of other atoms, molecules and ions. Generalization to the case of molecules requires the vibrational and rotational structure of the ion core to be taken into account, leading to several differences compared to the atomic case. More branches are expected to form because the electronic angular momenta also couple to the rotational angular momentum of the ion core following, typically, Hund's angular-momentum-coupling cases (d) or (e) [57]. Rotational and vibrational autoionization can occur and typically involve small energies for the ionized electron. If these decay channels dominate, we expect that the decay of the autoionization rates with ℓ be significantly slower. A comprehensive study of the autoionization of the high- ℓ Rydberg states of molecules is an interesting perspective for future work.

ACKNOWLEDGMENTS

We would like to thank F. Merkt for bringing the subject of the present paper to our attention, and X. Urbain for helpful comments. This work was supported by the Fonds de la Recherche Scientifique (FNRS) under IISN Grant No. 4.4504.10. E.M.B. and M.G. acknowledge support from the Fonds Spéciaux de Recherche (FSR) of

UCLouvain. Computational resources have been provided by the supercomputing facilities of the Université catholique de Louvain (CISM/UCL) and the Consortium des Équipements de Calcul Intensif en Fédération Wallonie Bruxelles (CÉCI) funded by the Fond de la Recherche Scientifique de Belgique (F.R.S.-FNRS) under

convention 2.5020.11 and by the Walloon Region.

Appendix A: Asymptotic formula for the angular integrals in jK coupling

In the perturbative limit and neglecting exchange, each multipole contribution $\Gamma^{(q)}$ to the total autoionization rate can be written in the jK coupling scheme as (see, *e.g.*, Refs. [20, 21] for details)

$$\Gamma^{(q)} = 2\pi \left[R_{N\ell_1 j_1}^{N' \ell'_1 j'_1, q} R_{n\ell}^{\varepsilon \ell', q} \right]^2 [\ell_1, \ell'_1, \ell, \ell', j_1, j'_1] \begin{pmatrix} \ell'_1 & q & \ell_1 \\ 0 & 0 & 0 \end{pmatrix}^2 \begin{pmatrix} \ell' & q & \ell \\ 0 & 0 & 0 \end{pmatrix}^2 \begin{Bmatrix} j_1 & q & j'_1 \\ \ell'_1 & 1/2 & \ell_1 \end{Bmatrix}^2 \begin{Bmatrix} \ell' & j'_1 & K \\ j_1 & \ell & q \end{Bmatrix}^2. \quad (\text{A1})$$

The symbols are defined as in Eq. (9). The limit of large ℓ values implies that K is large because j_1 is small. Because q is small, ℓ' is large and j'_1 is small. Using the symmetry of the $6j$ symbols and the asymptotic formula given in Ref. [55], the last squared Wigner $6j$ symbol in the above equation simplifies to

$$\begin{Bmatrix} \ell' & j'_1 & K \\ j_1 & \ell & q \end{Bmatrix}^2 \simeq \frac{\langle j_1 b j'_1 (\Delta\ell - b) | q \Delta\ell \rangle^2}{2\ell(2q+1)}. \quad (\text{A2})$$

We defined $b = K - \ell$, which labels in fact the autoionization branch (see Sec. III B). The quantity $\Delta\ell = \ell' - \ell$ represents the change in orbital angular momentum of the Rydberg electron upon autoionization. Using the symmetry properties of Clebsch-Gordan coefficients one can rewrite the above equation as

$$\begin{Bmatrix} \ell' & j'_1 & K \\ j_1 & \ell & q \end{Bmatrix}^2 \simeq \frac{\langle j_1 b q (-\Delta\ell) | j'_1 (b - \Delta\ell) \rangle^2}{2\ell(2j'_1 + 1)}. \quad (\text{A3})$$

The square of the $3j$ symbol involving ℓ and ℓ' in Eq. (A1) can also be simplified in the limit $\ell, \ell' \gg q$. Using the asymptotic expression for Clebsch-Gordan coefficients of Ref. [58], we have

$$\begin{pmatrix} \ell' & q & \ell \\ 0 & 0 & 0 \end{pmatrix}^2 \simeq \frac{[D_{0\Delta\ell}^q(0, \frac{\pi}{2}, 0)]^2}{2\ell' + 1}, \quad (\text{A4})$$

where $D_{0\Delta\ell}^q(0, \frac{\pi}{2}, 0)$ is the Wigner D matrix. Replacing Eqs. (A3) and (A4) in Eq. (A1), one obtains

$$\Gamma^{(q)} = 2\pi \left[R_{N\ell_1 j_1}^{N' \ell'_1 j'_1, q} R_{n\ell}^{\varepsilon \ell', q} \right]^2 [\ell_1, \ell'_1, j_1] \begin{pmatrix} \ell'_1 & q & \ell_1 \\ 0 & 0 & 0 \end{pmatrix}^2 \begin{Bmatrix} j_1 & q & j'_1 \\ \ell'_1 & 1/2 & \ell_1 \end{Bmatrix}^2 \langle j_1 b q (-\Delta\ell) | j'_1 (b - \Delta\ell) \rangle^2 [D_{0\Delta\ell}^q(0, \frac{\pi}{2}, 0)]^2, \quad (\text{A5})$$

where we used $2\ell + 1 \simeq 2\ell$. The angular part of this equation, *i.e.*, the terms on the right hand side that depend

on the angular-momentum quantum numbers, is the one given in Eq. (17).

- [1] P. Camus, T. F. Gallagher, J. M. Lecomte, P. Pillet, L. Pruvost, and J. Boulmer, *Phys. Rev. Lett.* **62**, 2365 (1989).
- [2] J. B. M. Warntjes, C. Wesdorp, F. Robicheaux, and L. D. Noordam, *Phys. Rev. Lett.* **83**, 512 (1999).
- [3] D. Wehrli, M. Génévriez, and F. Merkt, *Phys. Rev. A* **100**, 012515 (2019).

- [4] W. E. Cooke, T. F. Gallagher, S. A. Edelstein, and R. M. Hill, *Phys. Rev. Lett.* **40**, 178 (1978).
- [5] E. Luc-Koenig, M. Aymar, R. Van Leeuwen, W. Ubachs, and W. Hogervorst, *Phys. Rev. A* **52**, 208 (1995).
- [6] M. Aymar, C. H. Greene, and E. Luc-Koenig, *Rev. Mod. Phys.* **68**, 1015 (1996).
- [7] S. N. Pisharody and R. R. Jones, *Science* **303**, 813 (2004).

- [8] U. Eichmann, V. Lange, and W. Sandner, *Phys. Rev. Lett.* **68**, 21 (1992).
- [9] R. R. Jones and T. F. Gallagher, *Phys. Rev. A* **42**, 2655 (1990).
- [10] M. Génévriez and U. Eichmann, *Phys. Rev. A* **107**, 012817 (2023).
- [11] G. Fields, X. Zhang, F. B. Dunning, S. Yoshida, and J. Burgdörfer, *Phys. Rev. A* **97**, 013429 (2018).
- [12] M. Génévriez, *Mol. Phys.* **119**, e1861353 (2021).
- [13] S. Yoshida, J. Burgdörfer, R. Brienza, G. Fields, and F. B. Dunning, *Phys. Rev. A* **107**, 043112 (2023).
- [14] M. Génévriez, C. Rosen, and U. Eichmann, *Phys. Rev. A* **104**, 012812 (2021).
- [15] T. F. Gallagher, *Rydberg Atoms* (Cambridge University Press, Cambridge, 1994).
- [16] F. Roussel, M. Cheret, L. Chen, T. Bolzinger, G. Spiess, J. Hare, and M. Gross, *Phys. Rev. Lett.* **65**, 3112 (1990).
- [17] H. Lehec, X. Hua, P. Pillet, and P. Cheinet, *Phys. Rev. A* **103**, 022806 (2021).
- [18] R. C. Teixeira, A. Larrouy, A. Muni, L. Lachaud, J.-M. Raimond, S. Gleyzes, and M. Brune, *Phys. Rev. Lett.* **125**, 263001 (2020).
- [19] R. R. Jones and T. F. Gallagher, *Phys. Rev. A* **38**, 2846 (1988).
- [20] M. Poirier, *Phys. Rev. A* **38**, 3484 (1988).
- [21] M. Poirier, *Phys. Rev. A* **50**, 1335 (1994).
- [22] G. Reiser, W. Habenicht, K. Müller-Dethlefs, and E. W. Schlag, *Chem. Phys. Lett.* **152**, 119 (1988).
- [23] F. Merkt, S. Willitsch, and U. Hollenstein, in *Handbook of High-resolution Spectroscopy* (Wiley, 2011) pp. 1617–1654.
- [24] W. A. Chupka, *J. Chem. Phys.* **98**, 4520 (1993).
- [25] U. Hollenstein, R. Seiler, H. Schmutz, M. Andrist, and F. Merkt, *J. Chem. Phys.* **115**, 5461 (2001).
- [26] D. Wehrli, M. Génévriez, and F. Merkt, *Phys. Chem. Chem. Phys.* **23**, 10978 (2021).
- [27] G. Lochead, D. Boddy, D. P. Sadler, C. S. Adams, and M. P. A. Jones, *Phys. Rev. A* **87**, 053409 (2013).
- [28] J. Millen, G. Lochead, and M. P. A. Jones, *Phys. Rev. Lett.* **105**, 213004 (2010).
- [29] I. S. Madjarov, J. P. Covey, A. L. Shaw, J. Choi, A. Kale, A. Cooper, H. Pichler, V. Schkolnik, J. R. Williams, and M. Endres, *Nat. Phys.* **16**, 857 (2020).
- [30] R. Mukherjee, J. Millen, R. Nath, M. P. A. Jones, and T. Pohl, *J. Phys. B: At. Mol. Opt. Phys.* **44**, 184010 (2011).
- [31] P. McQuillen, X. Zhang, T. Strickler, F. B. Dunning, and T. C. Killian, *Phys. Rev. A* **87**, 013407 (2013).
- [32] A. Muni, L. Lachaud, A. Couto, M. Poirier, R. C. Teixeira, J.-M. Raimond, M. Brune, and S. Gleyzes, *Nat. Phys.* **18**, 502 (2022).
- [33] K.-L. Pham, T. F. Gallagher, P. Pillet, S. Lepoutre, and P. Cheinet, *PRX Quantum* **3**, 020327 (2022).
- [34] A. P. Burgers, S. Ma, S. Saskin, J. Wilson, M. A. Alarcón, C. H. Greene, and J. D. Thompson, *PRX Quantum* **3**, 020326 (2022).
- [35] M. Génévriez, D. Wehrli, and F. Merkt, *Phys. Rev. A* **100**, 032517 (2019).
- [36] J. E. Hansen, C. Laughlin, H. W. van der Hart, and G. Verboeckhaven, *J. Phys. B: At. Mol. Opt. Phys.* **32**, 2099 (1999).
- [37] E. Luc-Koenig, M. Aymar, J.-M. Lecomte, and A. Lyras, *J. Phys. B: At. Mol. Opt. Phys.* **31**, 727 (1998).
- [38] E. Luc-Koenig, A. Lyras, J.-M. Lecomte, and M. Aymar, *J. Phys. B: At. Mol. Opt. Phys.* **30**, 5213 (1997).
- [39] C. A. Nicolaides and D. R. Beck, *Phys. Lett. A* **65**, 2 (1978).
- [40] B. Simon, *Phys. Lett. A* **71**, 211 (1979).
- [41] J. Eiglsperger, B. Piraux, and J. Madroñero, *Phys. Rev. A* **80**, 022511 (2009).
- [42] T. N. Rescigno and C. W. McCurdy, *Phys. Rev. A* **62**, 032706 (2000).
- [43] D. Manolopoulos and R. Wyatt, *Chem. Phys. Lett.* **152**, 23 (1988).
- [44] E. Y. Xu, Y. Zhu, O. C. Mullins, and T. F. Gallagher, *Phys. Rev. A* **33**, 2401 (1986).
- [45] A. Bolovinos, E. Luc-Koenig, S. Assimpoulos, A. Lyras, N. E. Karapanagioti, D. Charalambidis, and M. Aymar, *Z. Phys. D* **38**, 265 (1996).
- [46] G. W. Schinn, C. J. Dai, and T. F. Gallagher, *Phys. Rev. A* **43**, 2316 (1991).
- [47] C. J. Dai, G. W. Schinn, and T. F. Gallagher, *Phys. Rev. A* **42**, 223 (1990).
- [48] E. Y. Xu, Y. Zhu, O. C. Mullins, and T. F. Gallagher, *Phys. Rev. A* **35**, 1138 (1987).
- [49] S. Assimpoulos, A. Bolovinos, A. Jimoyiannis, P. Tsekeris, E. Luc-Koenig, and M. Aymar, *J. Phys. B: At. Mol. Opt. Phys.* **27**, 2471 (1994).
- [50] A. Jimoyiannis, A. Bolovinos, and P. Tsekeris, *Z Phys D - Atoms, Molecules and Clusters* **22**, 577 (1992).
- [51] R. D. Cowan, *The Theory of Atomic Structure and Spectra*, Los Alamos Series in Basic and Applied Sciences (University of California Press, Berkeley, 1981).
- [52] A. Matsumoto, *Phys. Scr.* **44**, 154 (1991).
- [53] The mpmath development team, Mpmath: A Python library for arbitrary-precision floating-point arithmetic (version 1.3.0) (2023).
- [54] H. A. Bethe and E. E. Salpeter, *Quantum Mechanics of One- and Two-Electron Atoms* (Springer-Verlag Berlin Heidelberg, Berlin, Heidelberg, 1957).
- [55] D. A. Varshalovich, A. N. Moskalev, and V. K. Khersonskii, in *Quantum Theory of Angular Momentum* (World Scientific, 1988) p. 264.
- [56] W. E. Cooke and T. F. Gallagher, *Phys. Rev. A* **19**, 2151 (1979).
- [57] H. Lefebvre-Brion and R. W. Field, in *The Spectra and Dynamics of Diatomic Molecules* (Elsevier, 2004) pp. 87–231.
- [58] D. A. Varshalovich, A. N. Moskalev, and V. K. Khersonskii, in *Quantum Theory of Angular Momentum* (World Scientific, 1988) p. 306.